ACS Catalysis

Research Article

pubs.acs.org/acscatalysis

Structure Sensitivity of Oxidative Dehydrogenation of Cyclohexane over FeO_x and Au/Fe_3O_4 Nanocrystals

S. Goergen,[†,∥] C. Yin,[‡,∥] M. Yang,[†] B. Lee,[§] S. Lee,[§] C. Wang,[†] P. Wu,[†] M. B. Boucher,[†] G. Kwon,[‡] S. Seifert,[§] R. E. Winans,[§] S. Vajda,*[,‡,⊥,¶] and M. Flytzani-Stephanopoulos*[,†]

[†]Department of Chemical and Biological Engineering, Tufts University, 4 Colby Street, Medford, Massachusetts 02155, United States

[‡]Materials Science Division, [§]X-ray Science Division, [⊥]Nanoscience and Technology Division, Argonne National Laboratory, 9700 South Cass Avenue, Argonne, Illinois 60439, United States

[¶]Department of Chemical and Environmental Engineering, Yale University, 9 Hillhouse Avenue, New Haven, Connecticut 06520, United States

ABSTRACT: Shape-controlled nanoscale FeO_x and Au/Fe_3O_4 catalysts with an inverse spinel structure were prepared and tested for the oxidative dehydrogenation of cyclohexane. The reaction was studied in situ in SAXS/TPRx mode with isothermal steady-state holds. {111}-Bound Fe_3O_4 nanooctahedra are highly stable under reaction conditions at 300 °C, but {100}-bound nanocubes begin to agglomerate above 250 °C. The selectivity to cyclohexene and benzene over CO_2 depends strongly on the iron oxide shape and its interaction with the gold. When gold is added onto the iron oxide, the formation of benzene over cyclohexene is favored over both shapes. The highest benzene yield was measured on the Au/Fe_3O_4 octahedra. A parallel study of a commercial polycrystalline Au/Fe_2O_3 powder was conducted, and the activity and selectivity of this catalyst were compared with the nanoshapes. After leaching of the gold with a sodium cyanide solution and heat treatment, the atomically dispersed gold on the iron oxide surface selectively catalyzed the ODH of cyclohexane to benzene. Stabilization of cationic gold was found by in situ XANES conducted during the ODH reaction.

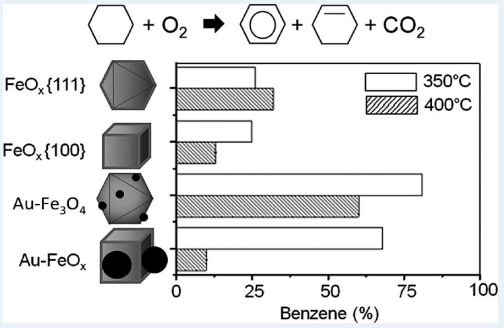

KEYWORDS: *gold, iron oxide, oxidative dehydrogenation, cyclohexane, shape effect, benzene, structure selectivity*

1. INTRODUCTION

The dehydrogenation of cyclohexane to cyclohexene and benzene is an important process for the production of chemicals and polymers. The heterogeneously catalyzed reaction is typically carried out at high temperatures in anaerobic conditions. A stepwise removal of hydrogen leads to the formation of cyclohexene and eventually to benzene. The breakage of C−H bonds is the rate-limiting step of the dehydrogenation reaction and competes with the scission of C−C and C═C bonds. The secondary production of hydrocarbon fragments and coke causes deactivation of the catalyst. By adding hydrogen to the reactant stream, the hydrocarbon cracking can be largely suppressed.[1,2]

In recent years, oxidative dehydrogenation has been considered as a promising alternative to current industrial processes. Especially in the case of ethane and propane, considerable progress has been made.[3] The oxidative pathway is thermodynamically favored and proceeds at much lower temperatures. In the presence of oxygen, hydrogen is converted to water, and hydrocarbon fragments are recovered in the form of carbon oxides. Combustion largely prevents coke formation and, thus, catalyst deactivation.[4] Despite a growing research effort, however, catalyst design remains an important challenge to improve dehydrogenation activity and selectivity.

Platinum- and vanadia-based catalysts are well studied and among the most efficient for cyclohexane dehydrogenation.[5−8] A number of other materials include metal-doped zeolites and metal phosphates.[9−11] In recent years, gold nanoparticles supported on metal oxides have been shown to be attractive catalysts in a number of selective oxidation and hydrogenation reactions.[12,13] Their potential for oxidative dehydrogenation was pointed out by Bond as early as 1972.[14] More recently, the Hutchings group has reported that metal oxide-supported Au−Pd alloys are highly selective catalysts for the formation of benzene from cyclohexane and cyclohexene,[15] and Vajda and coworkers reported nanometer and subnanometer cobalt oxide catalysts for the same reaction.[16−18] Gold supported on various oxide supports, including iron oxide, has also been studied for the oxidative dehydrogenation of ethane, propane, 1-butene and α,ω-diols.[19−21]

Today, only little is understood regarding the relationship between the gold−metal oxide structures and their dehydrogenation activity. The addition of gold is generally observed to increase the activity and selectivity of metal oxides. The nature of

Received: November 23, 2012
Revised: January 31, 2013
Published: February 7, 2013

the underlying support, however, plays a crucial role in the catalyst performance. Metal oxide supports with high oxygen mobility in conjunction with closely contacted gold nanoparticles were found to favor the dehydrogenation reaction.[21] Sa et al. recently correlated the high dehydrogenation activity of gold−lanthanum oxide with the ability of lanthanum oxide to stabilize cationic gold at high temperatures.[20] In contrast to the anaerobic reaction, in which metallic clusters are believed to be the active sites,[10,11,22] cationic gold has been related to high alkene selectivity with low carbon oxide formation during the oxidative dehydrogenation of C_{2+} aliphatic alkanes.[20] Similarly, Vajda et al. reported an extraordinary activity of size-selected Pt_{8-10} clusters deposited on aluminum oxide surfaces for the oxidative dehydrogenation of propane. In comparison with conventional Pt and vanadia catalysts, the under-coordinated atoms in subnanometer Pt clusters were shown to favor C−H scission over the breakage of C−C and C═C bonds.[23]

Atomically dispersed gold species, strongly interacting with the metal oxide support, have been the focus for a number of other reactions.[24] Comparing parent and NaCN-leached gold-based catalysts, Fu et al. have discovered that atomically dispersed cationic gold species stabilized by ceria are the active sites for the water-gas shift reaction.[25] Similar observations have been made in the case of gold/iron oxide catalysts, and the presence of a preponderance of isolated gold atoms has been verified by atomic resolution STEM.[26,27] In a first-of-a-kind catalytic study carried out with gold deposited on ceria single crystal nanoshapes, Si and Flytzani-Stephanopoulos have shown that the {110} surfaces of ceria provide more anchoring sites for atomically dispersing the gold and, hence, a better overall activity for the water-gas shift reaction.[28] The shape effect of ceria was demonstrated to be indirect, as the apparent activation energies of the reaction are the same for all shapes. It has further been shown that atomically dispersed gold with strong Au−O-M bonds forms only on CeO_2{110}/{111}, ZnO{1000}, and Fe_3O_4{111}surfaces, thus resulting in enhanced water-gas shift and methanol steam reforming reaction rates on these surfaces.[28,29]

In the present study, we apply a similar strategy to identify potential shape effects of gold/iron oxide catalysts for the oxidative cyclohexane dehydrogenation reaction. Nanoscale single crystal iron oxide supports with cubic and octahedral shapes, bound by {100} and {111} surfaces, respectively, were prepared and used as supports. Scanning tunneling microscopy and theoretical studies showing that positively charged gold atoms can be stabilized on Fe_3O_4 (111),[30] and Fe_3O_4 (100) surfaces[31] have already been reported. Shape-controlled catalysts are compared with a commercial, bulk Au/Fe_2O_3 catalyst obtained from the World Gold Council (WGC). Shape, size, and oxidation state of the catalysts were monitored in situ by SAXS and XANES.

2. EXPERIMENTAL SECTION

2.1. Catalyst Preparation. Shape-controlled FeO_x and Au/Fe_3O_4 catalysts were prepared as reported earlier.[29] Octahedral and cubic FeO_x nanocrystals were synthesized by thermal decomposition of iron oleate. Nanooctahedra were formed in the presence of tetraoctylammonium bromide, and sodium oleate-mediated preparations yielded nanocubes. The synthesis was carried out in a 9:1 mixture of 1-octadecene and diphenylether at a reflux temperature of 300 °C and applying a heating rate of 3 °C min^{-1}. Products were recovered and washed by sequential precipitation and resuspension in a 1:1 hexane/ethanol mixture. To remove the organic surfactants from the iron oxide surface, the final samples were suspended in a 10% aqueous tetramethylammonium hydroxide solution. The aqueous iron oxide suspension was purified by sequential precipitation and suspension in distilled water. A small amount of sodium hydroxide was added to facilitate recovering the iron oxide nanoparticles by centrifugation.

Gold (2 atom % per total Fe atom) was deposited on the iron oxide nanoparticles by deposition−precipitation in the presence of sodium hydroxide (DP-NaOH). To 100 mL of an aqueous suspension of iron oxide (4 mg mL^{-1}), 45 mg of $HAuCl_4 \cdot 3H_2O$ in 5 mL of distilled water was added dropwise to 100 mL of an aqueous suspension of iron oxide (4 mg mL^{-1}). The pH of the suspension was adjusted to 8−9 by addition of sodium hydroxide. The final sample was sonicated for 1 h, washed with hot water (70 °C) and dried in vacuum at 80 °C overnight.

2.2. Catalyst Characterization and Activity Tests. Transmission electron microscopy (TEM) was performed on a JEOL 200cx at 200 kV. For high-resolution imaging, a JEOL 2010 was used. Powder samples were suspended in ethanol via sonication, and a single drop of the corresponding suspension was applied to a carbon-film-coated copper grid. The average nanoparticle size was estimated from ∼100 nanoparticles. X-ray

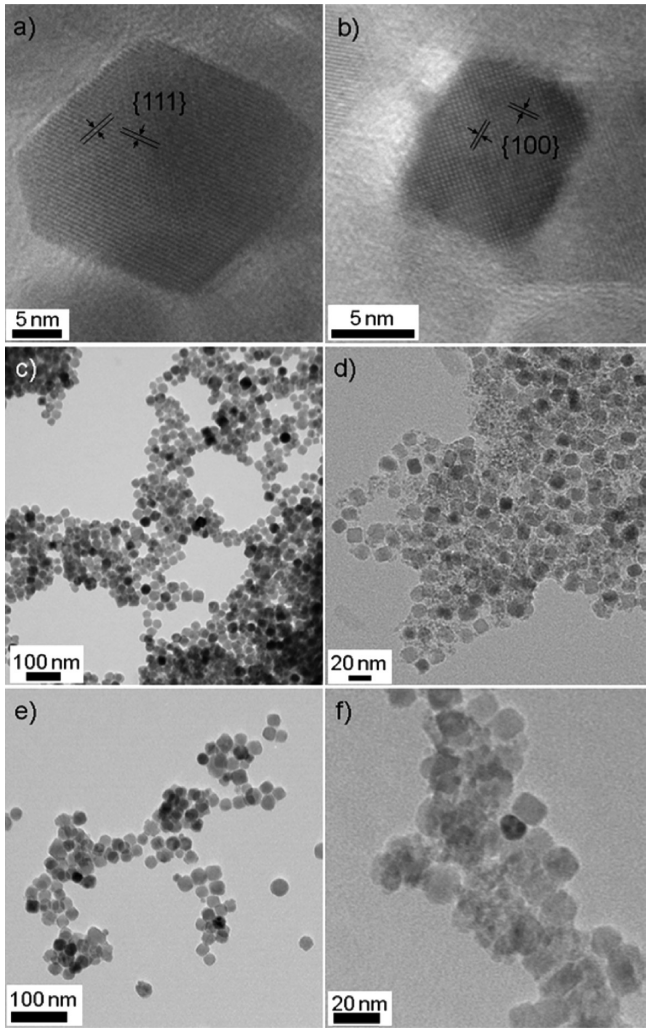

Figure 1. TEM images of as-synthesized catalysts: (a, c) FeO_x nanooctahedra, (b, d) FeO_x nanocubes, (e) Au/Fe_3O_4 nanooctahedra, and (f) Au/FeO_x nanocubes.

dx.doi.org/10.1021/cs3007582 | ACS Catal. 2013, 3, 529−539

diffraction (XRD) analysis was performed on a Rigaku 300 instrument with a rotating anode generator and a monochromatic detector. Cu Kα_1 radiation was used with a power setting of 50 kV and 250 mA. Typically, a scan rate of 2° min^{-1} with a 0.02° step size was used. Bulk elemental analysis of the samples was conducted by inductively coupled plasma optical emission spectrometry (ICP-OES, Leeman Laboratories Inc.). The BET surface area of the samples was determined by single-point N_2 adsorption/desorption cycles in a Micromeritics AutoChem 2920. The samples were pretreated in helium at 200 °C for 30 min.

In situ small-angle X-ray scattering (SAXS) experiments were conducted at the Advanced Photon Source at Argonne National Laboratory at beamline 12-ID-B and 12-ID-C. One-side-polished standard P-doped N-type silicon chips with a thickness of 300 μm were used as supports for the powder samples (MTI Corporation). The silicon chips were first cleaned with aqua regia (3:1 HCl/HNO_3), rinsed with ethanol, and calcined at 400 °C for 3 h. The iron oxide powders were suspended in ethanol (3 mg/mL) and drop-coated on the pretreated silicon chips. A loading of ~10 mg/chip was achieved. After deposition, the coated chip was dried at 80 °C in vacuum. The chip was loaded into a specially designed reaction cell, sealed with Kapton windows, and mounted on a computer-controlled goniometer.[32−37]

Table 1. Physicochemical Properties of FeO_x and Au−FeO_x Samples

sample	BET surface area (m^2 g^{-1}, Δ ± 5 m^2 g^{-1})	iron oxide nanoparticle size (nm, TEM, Δ ± 2 nm)	gold content (at. %, ICP, Δ ± 0.2%)
FeO_x octahedra	62	27	
Au/FeO_x octahedra	78	22	2.0
FeO_x cubes	103	12	
Au/FeO_x cubes	83	13	2.0
Au/Fe_2O_3 (WGC, parent)	44	15−60	2.0 (3.1 by XPS)
Au/Fe_2O_3 (WGC, NaCN-leached)	44	15−60	0.7 (0 by XPS)

Temperature-programmed oxidative cyclohexane dehydrogenation was conducted with a 0.4% cyclohexane/4% O_2 gas mixture in helium. The reaction cell was operated in a continuous flow mode at 800 Torr and at a flow rate of 30 mL min^{-1}. The temperature was increased from room temperature up to 300 °C with a heating rate of 10 °C min^{-1}. At 50 °C intervals, the temperature was held for 20 min to allow for steady state to be reached and SAXS data collection.

The gas composition at the cell outlet was analyzed using a differentially pumped mass spectrometer (Pfeiffer Vacuum Prisma Plus QMS 220 M2). An 12 keV X-ray beam with two-dimensional Pilatus 2 M (at 12-ID-B) or Platinum mosaic CCD (at 12-ID-C) detector was used for recording the SAXS images. A grazing-incidence geometry with an incidence angle of 0.1° was applied; however, information arising from the grazing-incidence geometry was compromised by the thickness of the sample layer on the silicon chip (>1 μm). Therefore, the collected data were handled similarly to transmission SAXS experiments. The 2-dimensional X-ray images were analyzed by taking cuts in the in-plane direction. To correlate the experimental line-cut data with theory, the X-ray scattering intensity, I, of randomly oriented particles was calculated as follows:

The scattering intensity of polyhedral particles in a powder sample is expressed by the following equation with use of the local monodisperse approximation:[38,39]

$$I(q) = I(0)(P(q)\,S(q) + n_{Au}\,P_{Au}(q)) \quad (1)$$

where q is the modulus of the scattering vector, $\mathbf{q}$;[39] $I(0)$ is the scaling factor, $I(q \to 0) = I(0)$; $P(q)$ is the orientation averaged form factor; and $S(q)$ is the structure factor. When particles are aggregated,

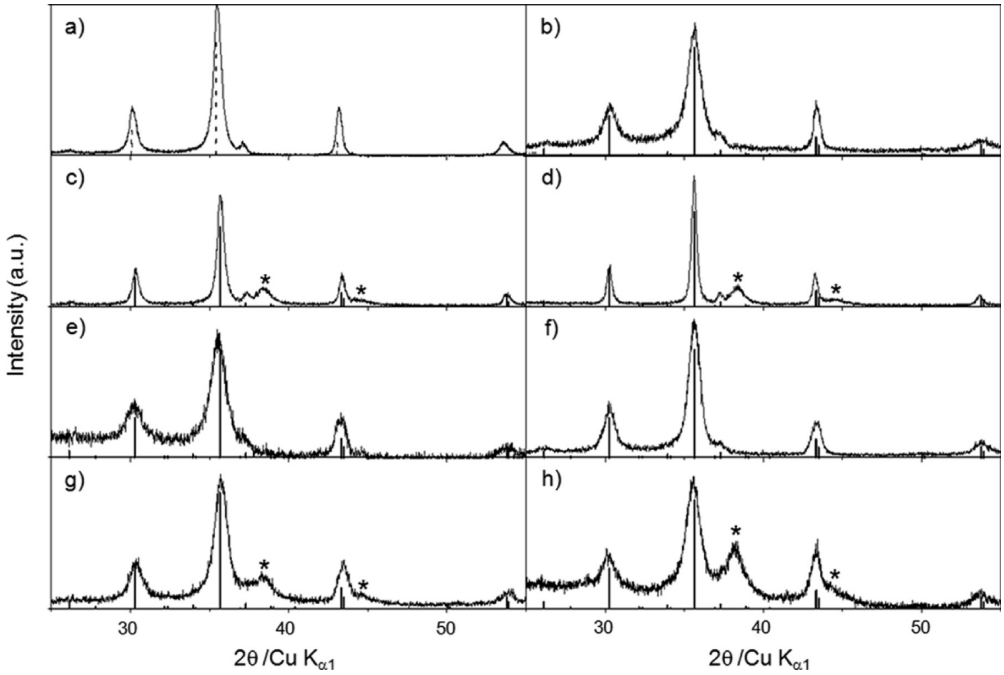

Figure 2. XRD pattern of as-synthesized and calcined catalysts: (a, b) FeO_x nanooctahedra, (c, d) Au/Fe_3O_4 nanooctahedra, (e, f) FeO_x nanocubes, (g, h) Au/FeO_x nanocubes; (a, c, e, g) as-synthesized, (b, d, f, h) calcined at 200 °C, – – Fe_3O_4 (PDF #01-077-1545), — γ-Fe_2O_3 (PDF #01-089-5894), * Au (PDF #04-004-5106).

dx.doi.org/10.1021/cs3007582 | ACS Catal. 2013, 3, 529−539

$$S(q) = cq^{-D_f} + S_h(q; R_h, \nu_f) \quad (2)$$

The first term serves to model the aggregates with parameters c and D_f, where c is a scaling constant, and D_f is the Porod power-law exponent for the aggregate.[40] The second term is the structure factor of homogenously distributed particles. In this work, it models the local structure in the aggregates. We used the structure factor derived from the PY hard sphere potential, of which parameters are the radius R_h and the volume fraction ν_f of the hard sphere.[38]

$P(q)$ of polydispersed polyhedra is calculated as follows:[39]

$$P(q) = \int n(r)\langle |F(\mathbf{q}, r)|^2 \rangle \, dr \quad (3)$$

where $n(r)$ is the size distribution function, which in this work is the Schultz distribution function.[38] $|F(\mathbf{q}, r)|^2$ is the form factor of the polyhedral particle whose size parameter is r, and $|F(0, r)|^2 = V(r)^2$, where $V(r)$ is the volume of the particle. r is the distance from the center of mass to a vertex of a polyhedron. The angled bracket indicates the orientation average, details of which can be found elsewhere.[39] When there are Au particles on the octahedron, the scattering function for them is added, as shown in eq 1, where n_{Au} is the number ratio of Au nanoparticles per octahedron, and the Au nanoparticle is modeled as a sphere with a polydispersity determined by the Schultz distribution function, too.

$$P_{Au}(q) = \int n(r)|F_s(q, r)|^2 \, dr \quad (4)$$

, where $|F_S(q, r)|^2$ is the form factor of a sphere with a radius r.

In situ Au and Fe XANES were employed to examine the oxidation states of the catalysts under reaction conditions. The spectra were collected using the beamline 12-BM of the Advanced Photon Source at Argonne National Laboratory. A 1 mg portion of the sample was loaded into a quartz capillary (1 mm in o.d.). The sample was kept in place by adding quartz wool at both ends. A gas mixture of 0.08% cyclohexane and 0.8% oxygen in helium was used, and a total flow rate of 5 mL min^{-1} was applied. The capillary was heated by two electrical resistances above and below the capillary, and the temperature was controlled by a thermocouple inside the capillary.[41] The samples were treated at various temperatures for 1 h and characterized at room temperature after cooling in the cyclohexane/oxygen gas mixture. Au XANES spectra were taken in the fluorescence mode with a 13-channel Ge detector. The detector was placed at 90° with respect to the incident beam, and the capillary was placed at 45° to both the incident beam and the Ge detector. The X-ray absorption edge energy at the Au L_{III} edge was calibrated by assigning the 11919 eV energy to the first inflection point in the XANES spectra of the metallic gold foil. A gold foil was used as the reference for Au^0 and $Au(OH)_3$ for Au^{3+}, respectively. Fe XANES spectra were taken in the transmission mode. The Fe K-edge was calibrated by assigning 7122 eV to the first inflection point in the XANES spectra. Fe_3O_4 and γ-Fe_2O_3 samples were used as reference. The reported XANES data are the averages of three scans (lasting ~11 min per scan). No changes were detected between the first and the last scan. The data were processed by the Athena program.[42]

Steady-state oxidative cyclohexane dehydrogenation experiments were performed in a fixed-bed quartz microreactor at atmospheric pressure. The gas composition of 0.4% cyclohexane/4% oxygen gas mixture in helium was the same as for the in situ reaction and SAXS tests described above. A 0.05 g portion of catalyst was mixed with 0.2 g of quartz sand. The catalyst was pretreated for 1 h at 200 °C in air. A total flow rate of 70 mL min^{-1} was applied. The temperature was increased from room temperature to 400 °C with a heating rate of 5 °C min^{-1}. The temperature was held for 1.5 h to reach steady-state conditions. The gas composition at the reactor outlet was analyzed by a mass spectrometer (MKS) and with a NDIR CO/CO_2 gas analyzer.

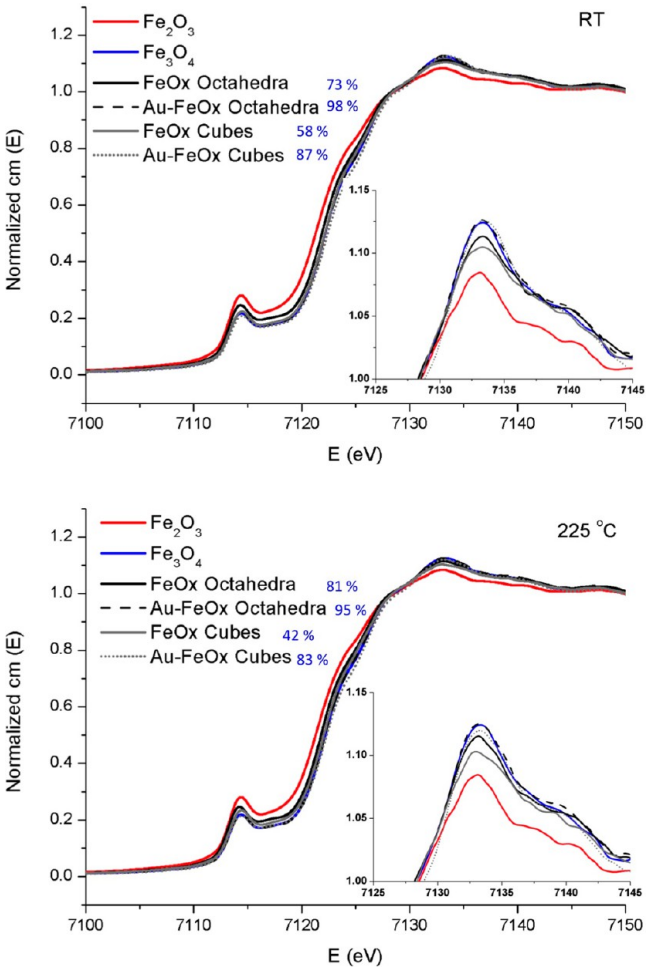

Figure 3. Fe K-edge fluorescence XANES spectra collected during oxidative dehydrogenation of cyclohexane with 0.08% cyclohexane/0.8% O_2 in helium. Fe_2O_3 and Fe_3O_4 are reference samples. The percentages indicate the content of Fe_3O_4 in the samples, which is obtained by linear combination using the Athena software.

3. RESULTS AND DISCUSSION

3.1. Characterization of Iron Oxide and Gold−iron Oxide Nanoshapes. Single crystal metal oxide nanoparticles with controlled shapes are excellent to investigate the relationship between catalyst structure and activity at atmospheric pressure. Shape-controlled and monodispersed iron oxide nanoparticles with sizes smaller than 50 nm are currently best synthesized by thermal decomposition of metal−organic precursors.[43] Thermolysis of iron oleate in the presence of tetraoctylammonium bromide is known to stimulate the preferential growth of nanooctahedra, and sodium oleate mediates the crystallization of nanocubes.[44] To use the iron oxide shapes as a catalyst support, we applied a treatment in aqueous tetramethylammonium hydroxide to remove the organic surfactant from the nanoparticle surface.[45] Final iron

dx.doi.org/10.1021/cs3007582 | ACS Catal. 2013, 3, 529−539

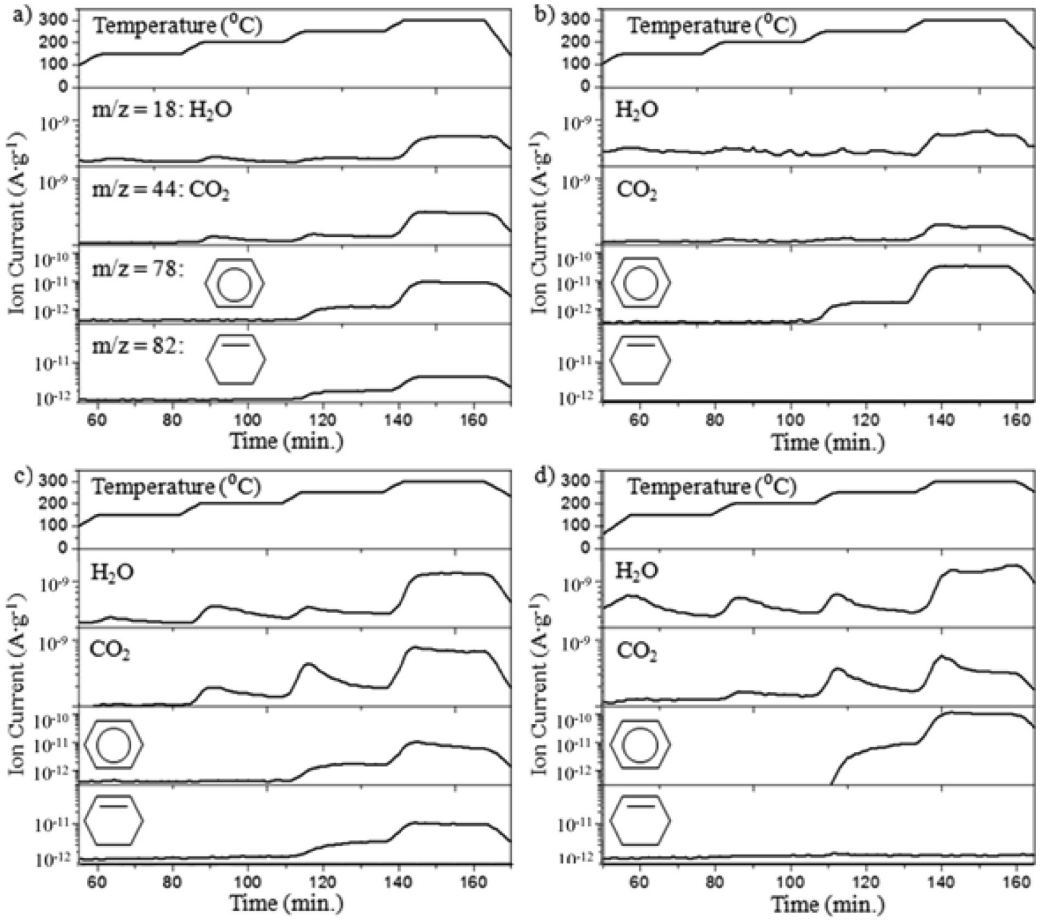

Figure 4. Temperature-programmed oxidative cyclohexane dehydrogenation (0.4% cyclohexane/4% O_2 in helium) with isothermal holds of 20 min each: (a) FeO_x octahedra, (b) Au/Fe_3O_4 octahedra, (c) FeO_x cubes, (d) Au/FeO_x cubes (data collected in the reaction cell with in situ SAXS analysis).

oxide samples are shown in Figure 1, and their physicochemical properties are summarized in Table 1. The nanocrystals have a specific surface area of 70−100 $m^2\ g^{-1}$. Both the cubic and octahedral nanoparticles were monodisperse, with average particle sizes of 12 (cubes) and 25 (octahedra) nm (Table 1). For nanooctahedra, the average particle size may vary from batch to batch between 15 and 30 nm. In contrast to nanocubes, the size-control of nanooctahedra was found to be sensitive to small variations in the experimental conditions. A different batch was used for gold deposition; hence, the difference in size for FeO_x and Au/FeO_x nanooctahedra. A size variation between 15 and 30 nm was not found to impact the oxidative dehydrogenation activity.

XRD patterns reveal that both iron oxide cubes and octahedra are formed of a cubic inverse spinel phase (Figure 2). Variations in diffraction intensities are primarily related to the amount of sample used for analysis. As can be seen in the high-resolution images of Figure 1, nanooctahedra are bound by {111} surface planes, and nanocubes are bound by {100} surface planes. The black color and the magnetic properties of the octahedra samples is in agreement with the Fe_3O_4 (magnetite) phase. A slight shift of the diffraction peaks toward lower 2θ values and a brownish hue of the cubic sample indicate the presence of a trace amount of γ-Fe_2O_3. After calcination in air at 200 °C, both iron oxide nanooctahedra and nanocubes have a red-brown color, and the position of XRD peaks is in agreement with the presence of γ-Fe_2O_3.

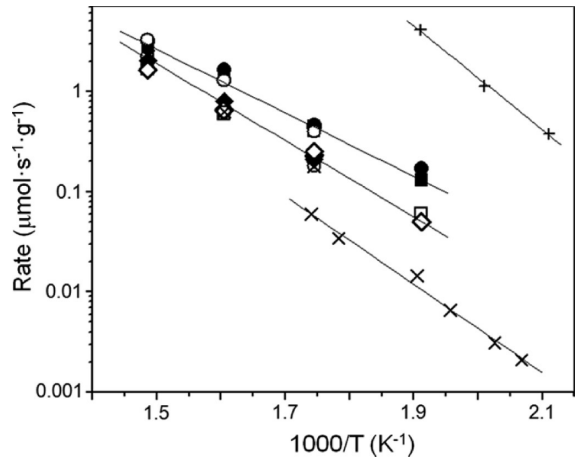

Figure 5. Steady-state reaction rates of oxidative dehydrogenation of cyclohexane: ◊, FeO_x octahedra; □, FeO_x cubes; ♦, Au/Fe_3O_4 octahedra; ■, Au/FeO_x cubes; ●, Au/Fe_2O_3 WGC (parent); ○, Au/Fe_2O_3 WGC (leached); ⊗, Au/Fe_2O_3 WGC (leached, reduced); +, 2.5% Au, 2.5% Pd−TiO_2 (ref 15); ×, $NiFe_2O_4$ (ref 41). Data collected from both the microreactor and the in situ SAXS reactor systems have been considered.

The resolution of these conventional characterization techniques makes it difficult to discriminate between the Fe_3O_4 and γ-Fe_2O_3 phases, which have very similar atomic plane spacings. For this purpose, qualitative Fe K-edge XANES analysis

dx.doi.org/10.1021/cs3007582 | ACS Catal. 2013, 3, 529−539

Table 2. Activity of Metal Oxide Catalysts for the Oxidative Dehydrogenation of Cyclohexane

sample	O_2/C_6H_{12} molar ratio	conversion (%)				activation energy (kJ mol^{-1})	ref
		250 °C	300 °C	350 °C	400 °C		
FeO_x octahedra	10	2	7	18	45	66 ± 3	this work
Au/Fe_3O_4 octahedra	10	1	6	22	56	73 ± 7	this work
FeO_x cubes	10	2	6	16	45	64 ± 4	this work
Au/FeO_x cubes	10	3	11	38	75	61 ± 3	this work
Au/Fe_2O_3 (WGC, parent)	10	2	12	45	87	60 ± 6	this work
Au/Fe_2O_3 (WGC, NaCN-leached)	10		11	35	89	67 ± 3	this work
Au/Fe_2O_3 (WGC, NaCN-leached, reduced in 5% H_2 at 200 °C)	10		5	17	61	80 ± 3	this work
Co_3O_4, 12 nm cubes	10					54	16
$NiFe_2O_4$	2					84	45
$NiCo_2O_4$	2					59	45
2.5% Au, 2.5% Pd−TiO_2	2.5					98	15
VO_x/Al_2O_3	2					63−107	47
V_2O_5/SiO_2	1−2					83−88	11
V_2O_5−Nb_2O_5/SiO_2	0.5−2					71−92	11
vanadium phosphate	0.6					50	11
iron phosphate	0.6					77	11
cerium phosphate	0.6					88	11
H-ZSM-5	0.5−10					59−71	11
Co-ZSM-5	0.5−1					90−136	11

Table 3. Properties of FeO_x and Au−FeO_x Nanoparticles Obtained from SAXS Analyses

sample	temp (°C)	SAXS fitting parameters (Å^2)[a]					surface area	
		model	r_1	Δ_1	r_2	Δ_2	(Å^2/particle)[b]	(m^2 g^{-1})[c]
FeO_x octahedra	25	octahedron	143	15			$3.2\cdot10^5$	56
	300	octahedron	142	14			$3.2\cdot10^5$	56
$AuFe_3O_4$ octahedra	25	two-particle	111	11	5.0	0.2	$3.5\cdot10^5$	124
	300	two-particle	113	9	5.0	0.2	$3.5\cdot10^5$	124
	300	octahedron	113	9				
FeO_x cubes	25	cube	55	6			$1.0\cdot10^5$	147
	300	cube	57	7			$8.8\cdot10^4$	114
	400	cube	60	7				
Au/FeO_x cubes	25	cube	64	8			$1.2\cdot10^5$	107
	300	cube	62	8			$1.1\cdot10^5$	110
	400	sphere	67	31				

[a] r = half edge length in the case of cubes and octahedra and the radius in the case of spheres. Δ = width of the size distribution. r_1, Δ_1: iron oxide. r_2, Δ_2: gold. [b] Calculated from the Porod law (eq 8) [c] Calculated, assuming a particle density of $5\cdot10^{-24}$ Å^3 g^{-1}.

was carried out at room temperature and at 225 °C in a cyclohexane/oxygen atmosphere (Figure 3). The Fe K-edge features originate from the transition of 1s electrons to empty 3d and 4p orbitals. The small pre-edge peak is characteristic for 1s → 3d transitions for iron atoms in a tetrahedral environment. Since 1s → 3d transitions are symmetry-forbidden in the case of octahedral coordinated iron, this feature is characteristic of the spinel structure. The absorption maximum around 7133 eV has a higher intensity in the case of Fe_3O_4 than for γ-Fe_2O_3, reflecting the change in oxidation state.[46,47] The absorption maxima of all iron oxide samples are situated between the two reference samples, indicating the presence of both Fe_3O_4 and γ-Fe_2O_3. The ratio of Fe_3O_4 phase in each iron oxide and the gold/iron oxide nanoshapes is estimated by the linear combination results of the references through Athena software, and the Fe_3O_4 percentages are shown in Figure 3 following each sample name.

Gold (2 at. %) was deposited by DP-NaOH on both the iron oxide nanocubes and nanooctahedra. After gold deposition, the specific surface areas remained unchanged (Table 1). TEM did not show any gold nanoparticles on the iron oxide nanooctahedra or nanocube surfaces (Figure 1), but the presence of small subnanometer clusters cannot be excluded, considering the TEM resolution. In recent work, the gold atoms and subnanometer clusters on iron oxide were imaged by aberration-corrected High Angle Annular Dark Field (HAADF)/STEM.[30,31] Evidence for the presence of strongly interacting subnanometer clusters and cations of gold with the iron oxide surface was obtained from H_2-TPR. Indeed, low-temperature hydrogen reduction features indicate the presence of Au−O−Fe species on both the nanooctahedra and nanocubes, but in a much higher amount in the octahedral samples.[29] The presence of strongly bound gold species was confirmed by NaCN leaching. After treatment in a 0.05% NaCN solution, the gold was entirely removed from the nanocubes, but a small amount of gold was still present on the nanooctahedra, as confirmed by ICP analysis and by the absence or presence of gold by Au-XANES.

XRD analyses revealed the presence of some 10 nm, large, gold nanoparticles in both samples (Figure 2). Semiquantitative

dx.doi.org/10.1021/cs3007582 | ACS Catal. 2013, 3, 529−539

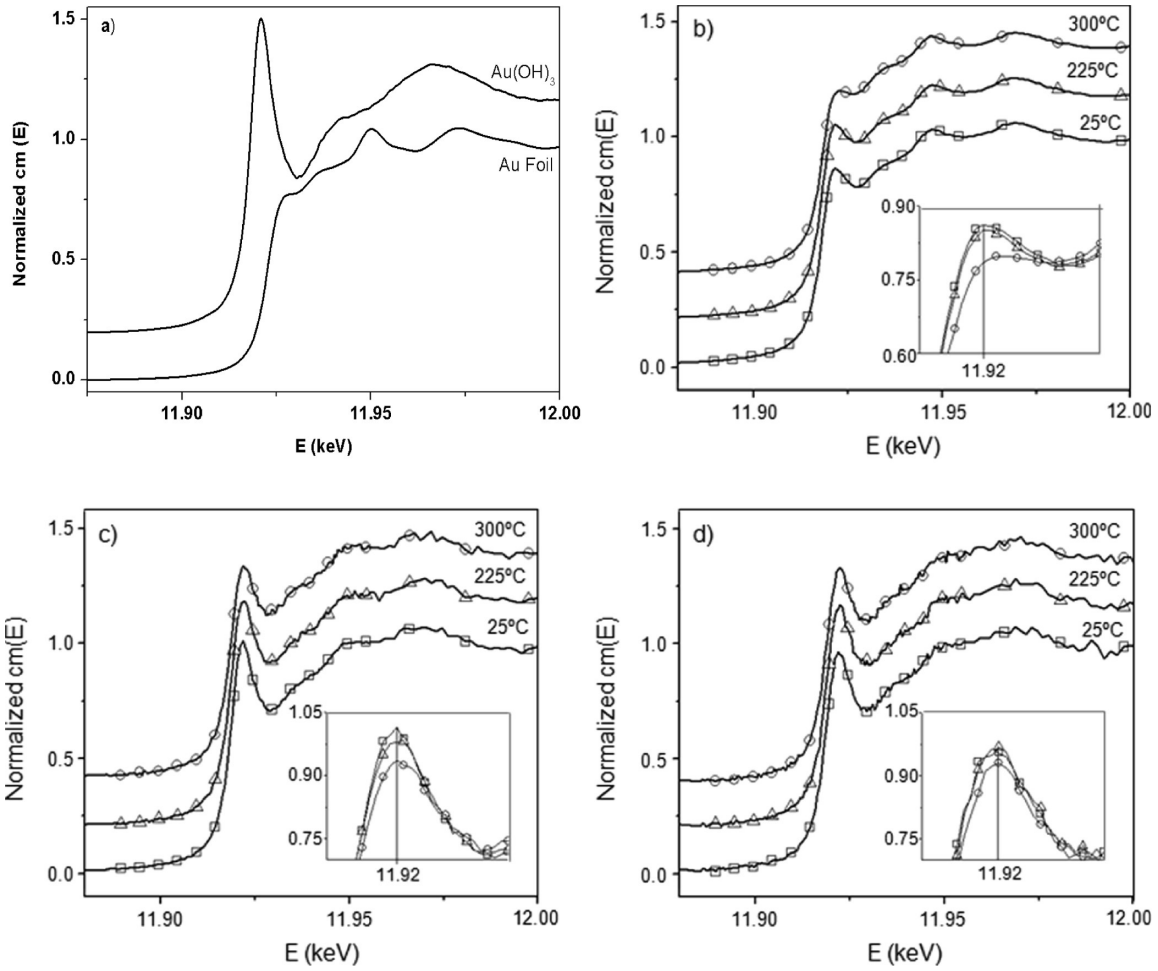

Figure 6. In situ Au L_{III} fluorescence XANES spectra collected during oxidative dehydrogenation of cyclohexane with 0.08% cyclohexane/0.8% O_2 in helium: (a) reference gold samples, (b) parent 5 wt % Au/Fe_2O_3 (WGC), (c) leached Au/Fe_2O_3 (WGC), and (d) Au/Fe_2O_3 (WGC) after NaCN leaching and reduction in 5% H_2 at 200 °C for 1 h.

estimates, based on reference intensity ratios, suggest that ~1 wt % of gold is present as metallic nanoparticles. Having the same dimension as the iron oxide support itself, these large nanoparticles are unlikely to interact strongly with the iron oxide surface. They can, of course, catalyze a different reaction pathway than the Au−O−Fe sites, and this is considered below.

Before and after calcination in air at 200 °C, the iron oxide is enriched in γ-Fe_2O_3. In oxidative reaction conditions over FeO_x and Au−FeO_x nanoshapes, γ-Fe_2O_3 is expected to remain stable. The Fe K-edge XANES spectra in Figure 3 show that the bulk composition of both Au−FeO_x nanoshapes is a mixture of Fe_3O_4 and Fe_2O_3, with the former phase dominating in the octahedra (Figure 3, Fe_3O_4 percentages labeled in blue). During reaction in a cyclohexane/oxygen atmosphere at 225 °C, the magnetite phase of the nanooctahedra is stable, while the nanocubes are partly oxidized into γ-Fe_2O_3. We may attribute these differences to the presence of gold, interacting stronger with the {111} surfaces, thus stabilizing the Fe_3O_4 phase.

3.2. Oxidative Dehydrogenation Activity and Selectivity. The catalytic activity for the oxidative cyclohexane dehydrogenation reaction was tested in a gas mixture of 4% O_2 and 0.4% cyclohexane in helium. Figure 4 shows the product formation as a function of temperature and time from the TPRx data collected in the reaction cell with in situ SAXS. An isothermal hold of 20 min at each temperature allowed the collection of the corresponding steady-state data. Cyclohexane is converted over the iron oxide and gold/iron oxide nanoshapes into cyclohexene, benzene, carbon dioxide, and water. For all samples studied, the dehydrogenation products started to appear above 200 °C. This temperature is typical for activation under oxidative conditions,[15,48] but it is low compared with the corresponding anaerobic processes. Both cyclohexene and benzene are formed over the iron oxide nanoshapes, but benzene is the only dehydrogenation product in the presence of gold. In the generally accepted hypothesis of a sequential reaction pathway, benzene is formed when the abstraction of additional hydrogen atoms from the olefinic intermediate is favored over the desorption of cyclohexene.[7,49] The addition of gold thus provides the necessary energy to further activate C−H bonds.

From the steady-state reaction data, an Arrhenius-type plot was constructed, as shown in Figure 5. It can be seen that the overall reaction rates per gram of catalyst are comparable for all samples studied. The activity is also very close to that of the reference 5 wt % Au−Fe_2O_3 catalyst obtained from the World Gold Council. However, if the rates are normalized with the surface area (Tables 1 and 3), they are higher (by ~50%) for the octahedral catalysts than the cubes. The rates for the FeO_x and Au/FeO_x samples studied in this work are higher than those for the $NiFe_2O_4$ catalysts reported by Turek et al.,[48] but are lower than the AuPd−TiO_2 catalyst studied by the Hutchings group,[15]

dx.doi.org/10.1021/cs3007582 | ACS Catal. 2013, 3, 529−539

as shown in Figure 5. The rates are also comparable to those reported for 12 nm Co_3O_4 nanocubes in the same gas composition as what is used here.[16] The apparent activation energies for the cyclohexane conversion over iron oxide and gold/iron oxide samples are in the range of 60−70 kJ mol^{-1} (Table 2). Slightly higher apparent activation energy is shown for the leached and prereduced commercial reference catalyst.

The evolution of the oxidation state of gold in reaction conditions was monitored by in situ XANES experiments using the commercial reference catalyst and leached samples thereof. We selected the reference sample over the nanoshapes because it contained more gold in its leached state and was thus conducive to the intended analysis. From the white-line intensity of the XANES spectra in Figure 6, it can be seen that the parent catalyst contains mostly metallic gold, whereas the leached catalysts before and after reduction contain primarily cationic gold. Mild reduction in H_2 helps to mobilize gold atoms from the iron oxide core to the surface without reducing it.[26] For the Au/Fe_2O_3 catalysts, Allard et al.[27,50] have shown that atomic gold species were strongly bound, even after redox heat treatments up to 673 K. In work with Au/Fe_3O_4 (111) single crystals, gold atoms over the uncapped O atoms were shown to be stable to 773 K.[30,51] The insets in Figure 6 show that the oxidation states of the catalysts do not change significantly during the oxidative dehydrogenation reaction. For all three samples, a small decrease of the intensity at the Au-L III absorption edge, due to a partial reduction of the cationic gold species, can be noticed.

Although the overall activity of FeO_x and Au/Fe_3O_4 samples is not significantly different, the catalyst structure has a strong impact on the benzene and carbon dioxide selectivity (Figure 7). This figure was constructed on the basis of selectivity at low conversions using the steady-state data of Table 2. As expected from thermal activation, the carbon dioxide selectivity increases while the benzene selectivity decreases with increasing temperature. The highest benzene selectivity is observed for the Au/Fe_3O_4 nanooctahedra. On Au/FeO_x nanocubes, the benzene selectivity is initially high, but decreases dramatically with increasing temperature. The carbon dioxide formation is lower on the octahedra than on the cubes, irrespective of the presence of gold. The ability of an oxide to work as a total oxidation catalyst is known to be related to the reducibility of the metal oxide. Highly reducible Mn_2O_3, for instance, converts cyclohexane into mainly carbon oxides.[11] Jin et al. also observed a similar relationship between the reducibility of mixed Mg−O−V catalysts and their selectivity for cyclohexane dehydrogenation and total oxidation.[52] The promotional effect of gold on the benzene selectivity of the iron oxide nanooctahedra observed here may be attributed to the interaction of gold with the iron oxide and the stabilization of the Fe_3O_4 phase by Au cations, as the XANES data in Figure 3 indicate. Under oxidative conditions, the γ-Fe_2O_3 phase will otherwise dominate. The addition of gold on the iron oxide nanocubes did not prevent their agglomeration upon heating to >250 °C, as found by the in situ SAXS experiments, discussed below, and this may have also contributed to their further loss of active Au−O−Fe sites and ensuing loss of selectivity to benzene at 400 °C (Figure 7d).

An alternative explanation for the increased selectivity of the gold-promoted iron oxide nanoshapes needs to be considered in view of the presence of weakly bound gold nanoparticles and clusters on their surfaces. This was addressed by considering the commercial reference 5 wt % $Au-Fe_2O_3$ (WGC) sample, which has a preponderance of gold nanoparticles on its surface.[23,24] This material catalyzes the complete combustion to CO_2, as can

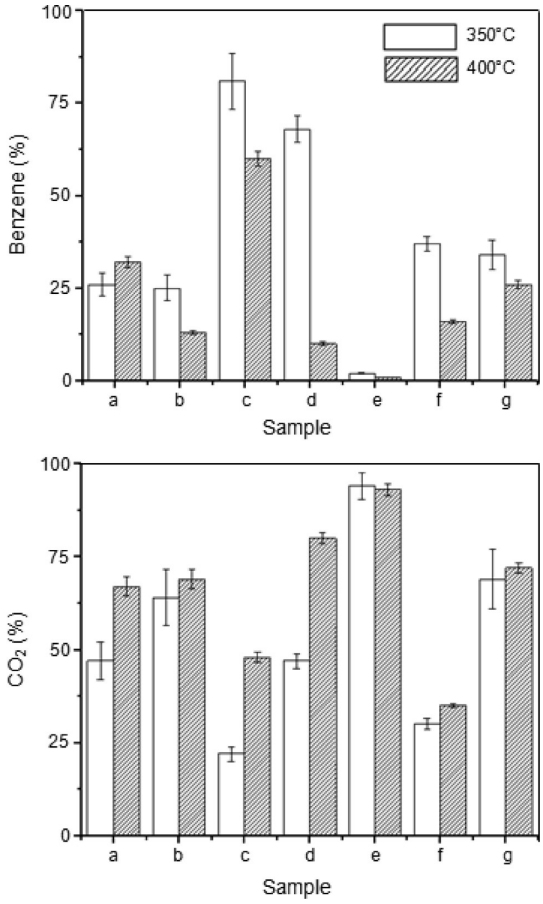

Figure 7. Product selectivity in the oxidative dehydrogenation of cyclohexane at the conditions of Figure 4 and from the fixed-bed experiments conducted in the microreactor (0.4% cyclohexane/4% O_2 in helium, steady-state data): (a) FeO_x octahedra, (b) FeO_x cubes, (c) Au/Fe_3O_4 octahedra, (d) Au/FeO_x cubes, (e) Au/Fe_2O_3 WGC (parent), (f) Au/Fe_2O_3 WGC (leached), and (g) Au/Fe_2O_3 WGC (leached, reduced).

be seen in Figure 7e. The metallic gold nanoparticles alone can be further ruled out as selective ODH sites by examining catalysts devoid of metallic gold after mild leaching with sodium cyanide solutions. The selectivities of the leached samples derived from the commercial 5 wt % $Au-Fe_2O_3$ (WGC) catalyst are different from the parent catalyst. Although the latter favors CO_2 (at >95%) at all temperatures, the leached samples show considerable selectivity to benzene. These samples comprise the residual gold as cations (Figure 6c and d) interacting with iron oxide as Au−O−Fe species.[26,27] Hence, we can conclude that Au−O−Fe species are responsible for the enhanced benzene selectivity and the metallic gold nanoparticles on the parent iron oxide sample catalyze the combustion reaction. In view of these findings, different preparation techniques should be examined in an effort to produce many more Au−O−Fe sites on the gold nanoshapes to achieve higher activity and, thus, higher benzene yields for potential practical application of these catalysts. The data collected here are useful in that they have identified an important trend: namely, it is possible to stabilize the active and selective Fe_3O_4 phase of iron oxide, even in excess oxygen atmospheres, by the addition of small amounts of gold through the formation of Au−O−Fe sites.

3.3. In Situ SAXS Characterization. The stability in size and shape of the iron oxide and gold/iron oxide nanoshapes in reaction conditions was probed by in situ SAXS experiments.

dx.doi.org/10.1021/cs3007582 | ACS Catal. 2013, 3, 529−539

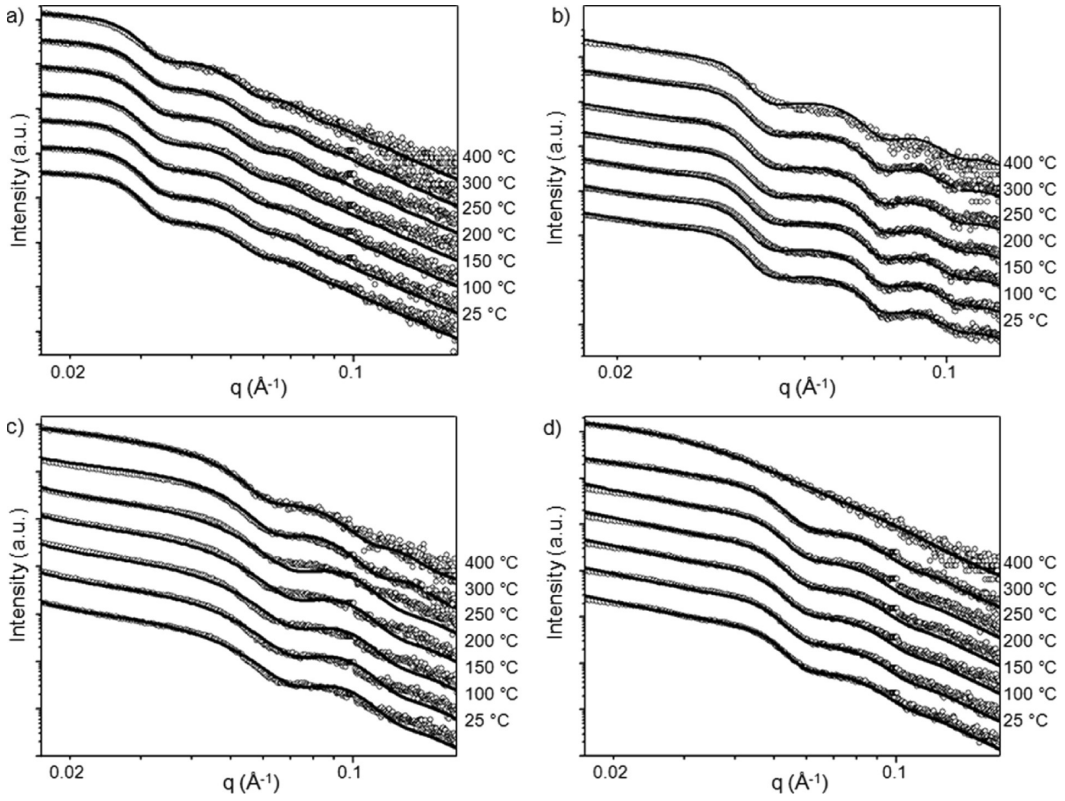

Figure 8. In situ SAXS characterization performed during oxidative cyclohexane dehydrogenation with 0.4% cyclohexane/4% O_2 in helium: (a) FeO_x octahedra, (b) Au/Fe_3O_4 octahedra, (c) FeO_x cubes, and (d) Au/FeO_x cubes. Fitting parameters are summarized in Table 3. The catalytic test at 400 °C was conducted ex situ over 90 min.

Figure 8 shows the $I(q)$ curves derived from scattering images collected at various temperatures. I is the scattering intensity, and q is the magnitude of the scattering vector. The X-ray scattering intensity originates primarily from the iron oxide support. Average particle sizes derived from the fitting of experimental $I(q)$ curves are summarized in Table 3. They are in good agreement with sizes obtained from TEM images (Table 1). Experimental data of iron oxide and gold/iron oxide are fitted using an octahedral model. For the gold-containing sample, the simple octahedral model does not match the experimental data in the high q region (Figure 9a). A two-particle model assuming subnanometer spherical particles on the octahedral surface describes reasonably well the experimental data (Figure 9b). The iron oxide and gold/iron oxide nanooctahedra are stable in reaction conditions up to 400 °C. No significant change in the position and slope of the oscillations in the scattering curves was observed (Figure 8a, b). The stability in shape and size is also confirmed by TEM (Figure 10a, b).

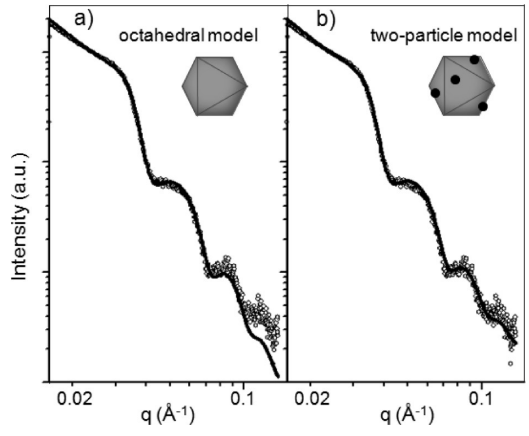

Figure 9. Comparison of two models for the fitting of experimental SAXS data for Au/Fe_3O_4 octahedra. Fitting parameters are summarized in Table 3.

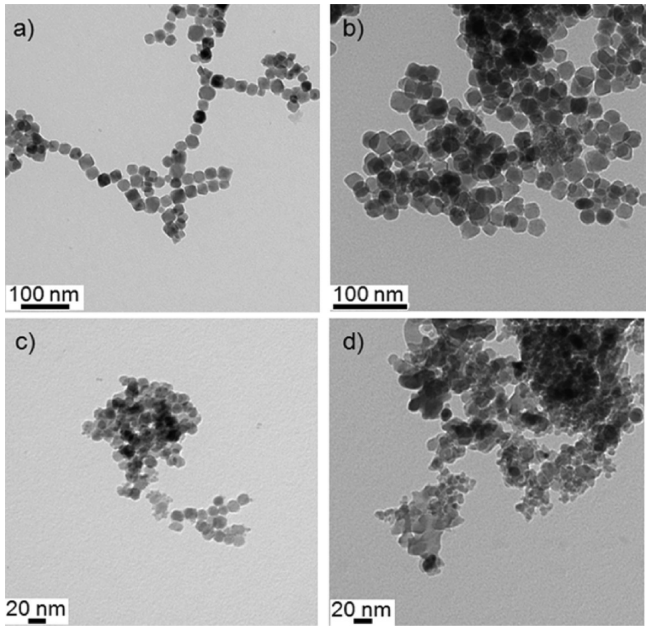

Figure 10. TEM images collected after oxidative dehydrogenation of cyclohexane at 400 °C for 90 min: (a) FeO_x octahedra, (b) Au/Fe_3O_4 octahedra, (c) FeO_x cubes, and (d) Au/FeO_x cubes.

dx.doi.org/10.1021/cs3007582 | *ACS Catal.* 2013, 3, 529−539

A simple cubic model accounts for the experimental data of both iron oxide and gold/iron oxide cubes. No clear difference was found among the data from those cubes. These results are in accordance with a lower Au−O−Fe interaction observed by hydrogen TPR.[29] For both cubic samples, the iron oxide support starts to change above 250 °C. The particle size of iron oxide nanocubes is stable up to 400 °C, but the $I(q)$ curves undergo a subtle change in the slope in the Porod region, where the $I(q)$ decrease as q^4, probably related to a change in the surface area (Figure 8c). According to the Porod law, the slope is proportional to the nanoparticle surface for large q, with

$$I(q) \rightarrow \frac{2\pi N(\Delta\rho)^2 S_p}{q^4} \quad (5)$$

where N, $\Delta\rho$ and S_p are the number of particles in the X-ray beam, the difference in electron density between a particle and its surrounding, and the surface area of the particle,[40] respectively. The Porod intensity (I_p) at large q can be defined as

$$I(q)\, q^4 \equiv I_p \quad (6)$$

A graphical representation of the Porod intensity as a function of q is shown in Figure 11.

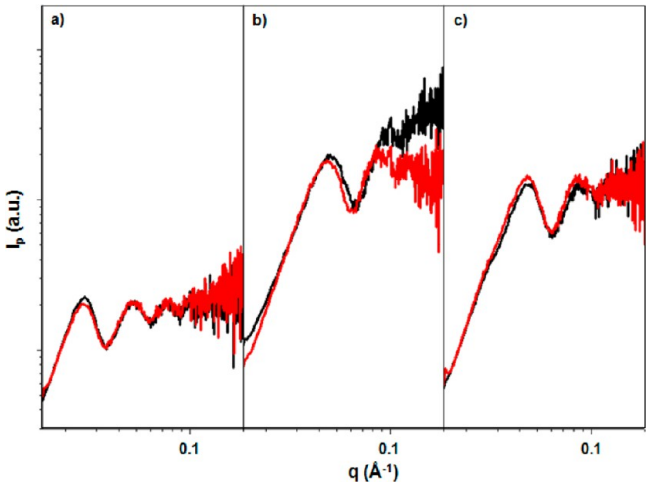

Figure 11. Porod plots corresponding to the $I(q)$ curves in Figure 8: (a) FeO_x octahedral, (b) FeO_x cubes, (c) Au/FeO_x cubes. Black, at 25 °C; red, at 300 °C.

From the Porod law and the relation below,

$$I(0) = N(\Delta\rho)^2 V_p^{\,2} \quad (7)$$

where V_p is the volume of the particle,

Finally, we get the relation

$$\frac{I_p}{I(0)} = \frac{2\pi S_p}{V_p^{\,2}} \quad (8)$$

.The surface areas, calculated according to eq 8, are summarized in Table 3. They are close to those measured by nitrogen physisorption and use of the BET equation (Table 1). Our calculations show that the surface area of the iron oxide cubes slightly decreases with increasing reaction temperature. The subtle change can probably be attributed to a transition from the cubic to a more stable, spherical shape. Note that when an ideal cube is transformed to an ideal sphere without changing the particle volume, the diameter of the sphere will be $(3/4\pi)^{3/2}2a$, where a is the edge length of the cube, and therefore, its surface area will decrease to 80.6%. The surface area of the bare iron oxide cube decreased to 88% with a minor size change. The nanoparticles displayed in Figure 8c have, indeed, a more rounded morphology. In contrast to the bare iron oxide support, the gold/iron oxide cubes start to sinter at 400 °C (Figure 8d). The particle distribution became polydispersed, as indicated by strongly damped oscillations. As a result, the particle size increased and the surface area per particle decreased, as shown in Table 3, indicating not only a shape change but also a volume increase via sintering. The TEM image in Figure 10d shows that the gold/iron oxide nanocubes had started to sinter with the formation of larger randomly shaped particles. The sintering of gold/iron oxide nanocubes was accompanied by a sharp drop in benzene selectivity (Figure 7d).

4. CONCLUSIONS

Iron oxide and gold/iron oxide nanooctahedra and nanocubes with a cubic inverse spinel structure are active catalysts for the oxidative dehydrogenation of cyclohexane with measurable activity at 200 °C. In situ SAXS experiments were useful in discriminating stable from unstable shapes due to heating in the reaction mixture. The nanocubes were unstable to heating above 250 °C, but Au addition suppressed this instability. Both cyclohexene and benzene dehydrogenation products are formed on the bare iron oxide nanoshapes, but the overall selectivity to them is low, the major product being CO_2. Addition of gold promotes the selectivity to benzene over cyclohexene, and suppresses the full combustion to CO_2. Selectivity to benzene exceeds 82% at 350 °C for the Au-promoted Fe_3O_4 nanooctahedra. The addition of gold is found to stabilize the Fe_3O_4 phase of iron oxide, presumably through Au−O−Fe sites that keep the iron oxide in the mixed oxidation state of Fe_3O_4, even in the presence of excess oxygen in the gas. The enhanced selectivity to benzene is not due to gold nanoparticles, as proved by the study of samples after removal of the gold nanoparticles by cyanide leaching.

Overall, the findings of this work establish for the first time the critical structural parameters that may be employed to tune the Fe_3O_4 catalyst activity and selectivity for the ODH of cyclohexane. Preparing and stabilizing atomically dispersed gold on the surface stabilizes the Fe_3O_4 phase and selectively produces benzene. This may be a general finding for the gold promotion of other oxide surfaces and for the dehydrogenation of other hydrocarbon molecules, as well, and warrants further investigation.

AUTHOR INFORMATION

Corresponding Author

*(M.F.-S.) Phone: (+1) 617-627-3048. Fax: (+1) 617-627-3991. E-mail: maria.flytzani-stephanopoulos@tufts.edu. (S.V.) E-mail: vajda@anl.gov.

Author Contributions

‖Equally contributing authors.

Notes

The authors declare no competing financial interest.

ACKNOWLEDGMENTS

The authors gratefully acknowledge financial support of this work by the Air Force Office of Scientific Research MURI program, Contract No. FA9559-08-1-0309. The work performed at Argonne was supported by the U.S. Department of Energy,

Office of Science, Office of Basic Energy Sciences, Materials Sciences under Contract No. DE-AC02-06CH11357. Use of the Advanced Photon Source, an Office of Science User Facility operated for the U.S. Department of Energy (DOE) Office of Science by Argonne National Laboratory, was supported by the U.S. DOE under Contract No. DE-AC02-06CH11357. S.G. gratefully acknowledges financial support from the National Research Fund, Luxembourg, cofunded under the Marie Curie Actions of the European Commission (FP7-COFUND).

REFERENCES

(1) Olah, G. A.; Molnar, A. *Hydrocarbon Chemistry*; Wiley-Interscience: New York, 1995.
(2) Bond, G.C. In *Metal-Catalyzed Reactions of Hydrocarbons*; Twigg, M. V., Spencer, M. S., Eds.; Springer: New York, 2005.
(3) Cavani, F.; Ballarini, N.; Cericola, A. *Catal. Today* **2007**, *127*, 113.
(4) Teschner, D.; Vass, E. M.; Schlogl, R. In *Metal Oxide Catalysis*; Jackson, S. D., Hargreaves, J. S. J., Eds.; Wiley-VCH: Weinheim, 2009.
(5) Briggs, R. A.; Taylor, H. S. *J. Am. Chem. Soc.* **1941**, *63*, 2500.
(6) Bridges, J. M.; Houghton, G. *J. Am. Chem. Soc.* **1959**, *81*, 1334.
(7) Kung, M. C.; Kung, H. H. *J. Catal.* **1991**, *128*, 287.
(8) Kariya, N.; Fukuoka, A.; Utagawa, T.; Sakuramoto, M.; Goto, Y.; Ichikawa, M. *Appl. Catal.* **2003**, *A 247*, 247.
(9) Mochida, I.; Jitsumatsu, T.; Kato, A.; Seiyama, T. *J. Catal.* **1975**, *36*, 361.
(10) Coughlan, B.; Keane, M. A. *Catal. Lett.* **1990**, *5*, 89.
(11) Panizza, M.; Resini, C.; Busca, G.; Fernandez Lopez, E.; Sanchez Escribano, V. *Catal. Lett.* **2003**, *89*, 199.
(12) Della Pina, C.; Falletta, E.; Prati, L.; Rossi, M. *Chem. Soc. Rev.* **2008**, *37*, 2077.
(13) McEwan, L.; Julius, M.; Roberts, S.; Fletcher, J. C. Q. *Gold Bull.* **2010**, *43*, 298.
(14) Bond, G. C. *Gold Bull.* **1972**, *5*, 11.
(15) Dummer, N. F.; Bawaked, S.; Hayward, J.; Jenkins, R.; Hutchings, G. J. *Catal. Today* **2010**, *154*, 2.
(16) Tyo, E. C.; Yin, C.; Di Vece, M.; Qian, Q.; Lee, S.; Lee, B.; Seifert, S.; Winans, R. E.; Si, R.; Ricks, B.; Goergen, S.; Flytzani-Stephanopoulos, M.; Wang, Z.; Palmer, R. E.; Neurock, M.; Vajda, S. *ACS Catal.* **2012**, *2*, 2409.
(17) Lee, S.; Di Vece, M.; Lee, B.; Seifert, S.; Winans, R. E.; Vajda, S. *ChemCatChem.* **2012**, *4*, 1632.
(18) Lee, S.; Di Vece, M.; Lee, B.; Seifert, S.; Winans, R. E.; Vajda, S. *Phys. Chem. Chem. Phys.* **2012**, *14*, 9336.
(19) Huang, J.; Dai, W. L.; Fan, K. *J. Phys. Chem. C* **2008**, *112*, 16110.
(20) Sa, J.; Ace, M.; Delgado, J. J.; Goguet, A.; Hardacre, C.; Morgan, K. *ChemCatChem* **2011**, *3*, 394.
(21) Xu, J.; Huang, J.; Liu, Y. M.; Cao, Y.; Li, Y. X.; Fan, K. N. *Catal. Lett.* **2011**, *141*, 198.
(22) Tetenyi, P.; Galsan, V. *Appl. Catal.* **2002**, *A 229*, 181.
(23) Vajda, S.; Pellin, M. J.; Greeley, J. P.; Marshall, C. L.; Curtiss, L. A.; Ballentine, G. A.; Elam, J. W.; Catillon-Mucherie, S.; Redfern, P. C.; Mehmood, F.; Zapol, P. *Nat. Mater.* **2009**, *8*, 213.
(24) Flytzani-Stephanopoulos, M.; Gates, B. *Annu. Rev. Chem. Biomol. Eng.* **2012**, *3*, 545.
(25) Fu, Q.; Saltsburg, H.; Flytzani-Stephanopoulos, M. *Science* **2003**, *301*, 935.
(26) Deng, W.; Carpenter, C.; Yi, N.; Flytzani-Stephanopoulos, M. *Top. Catal.* **2007**, *44*, 199.
(27) Allard, L. F.; Borisevich, A.; Deng, W.; Si, R.; Flytzani-Stephanopoulos, M.; Overbury, S. H. *J. Electron Microsc.* **2009**, *58*, 199.
(28) Si, R.; Flytzani-Stephanopoulos, M. *Angew. Chem., Int. Ed.* **2008**, *47*, 2884.
(29) Boucher, M. B.; Goergen, S.; Yi, N.; Flytzani-Stephanopoulos, M. *Phys. Chem. Chem. Phys.* **2011**, *13*, 2517.
(30) Rim, K. T.; Eom, D.; Liu, L.; Stolyarova, E.; Raitano, J. M.; Chan, S. W.; Flytzani-Stephanopoulos, M.; Flynn, G. W. *J. Phys. Chem. C* **2009**, *113*, 10198.
(31) Spiridis, N.; Soche, R. P.; Handke, B.; Haber, J.; Szczepanik, M.; Korecki, J. *Catal. Today* **2011**, *169*, 24.
(32) Lee, S.; Molina, L. M.; María, M. L.; López, J.; Alonso, J. A.; Hammer, B.; Lee, B.; Seifert, S.; Winans, R. E.; Elam, J. W.; Pellin, M. J.; Vajda, S. *Angew. Chem., Int. Ed.* **2009**, *48*, 1467.
(33) Vajda, S.; Lee, S.; Sell, K.; Barke, I.; Kleibert, A.; von Oeynhausen, V.; Meiwes-Broer, K. H.; Fraile-Rodriguez, A.; Elam, J. W.; Pellin, M. J.; Lee, B.; Seifert, S.; Winans, R. E. *J. Chem. Phys.* **2009**, *131*, 121104.
(34) Lei, Y.; Mehmood, F.; Lee, S.; Greeley, J. P.; Lee, B.; Seifert, S.; Winans, R. E.; Elam, J. W.; Meyer, R. J.; Redfern, P. C.; Teschner, D.; Schlögl, R.; Pellin, M. J.; Curtiss, L. C.; Vajda, S. *Science* **2010**, *328*, 224.
(35) Wyrzgol, S. A.; Schäfer, S.; Lee, S.; Lee, B.; Di Vece, M.; Li, X.; Seifert, S.; Winans, R. E.; Stutzmann, M.; Lercher, J. A.; Vajda, S. *Phys. Chem. Chem. Phys.* **2010**, *12*, 5585.
(36) Molina, L. M.; Lee, S.; Sell, K.; Barcaro, G.; Fortunelli, A.; Lee, B.; Seifert, S.; Winans, R. E.; Elam, J. W.; Pellin, M. J.; Barke, I.; Kleibert, A.; von Oeynhausen, V.; Lei, Y.; Meyer, R. J.; Alonso, J. A.; Fraile-Rodríguez, A.; Giorgio, S.; Henry, C. R.; Meiwes-Broer, K. H.; Vajda, S. *Catal. Today* **2011**, *160*, 116.
(37) Lee, S.; Lee, B.; Seifert, S.; Vajda, S.; Winans, R. E. *Nucl. Instrum. Methods Phys. Res., Sect. A* **2011**, *649*, 200.
(38) Kotlarchyk, M.; Chen, S. H. *J. Chem. Phys.* **1983**, *79*, 2461.
(39) Jones, M. R.; Macfarlane, R. J.; Lee, B.; Zhang, J.; Young, K. L.; Senesi, A. J.; Mirkin, C. A. *Nat. Mater.* **2010**, *9*, 913.
(40) Roe, R.J. *Methods of X-ray and Neutron Scattering in Polymer Science*; Oxford University Press: New York, 2000.
(41) Chupas, P. J.; Chapman, K. W.; Kurtz, C.; Hanson, J. C.; Lee, P. L.; Grey, C. P. *J. Appl. Crystallogr.* **2008**, *41*, 822.
(42) Ravel, B.; Newville, M. *J. Synchrotron Radiat.* **2005**, *12*, 537.
(43) Park, J. N.; An, K. J.; Hwang, Y. S.; Park, J. G.; Noh, H. J.; Kim, J. Y.; Park, J. H.; Hwang, N. M.; Hyeon, T. H. *Nat. Mater.* **2004**, *3*, 891.
(44) Shavel, A.; Liz-Marzan, L. M. *Phys. Chem. Chem. Phys.* **2009**, *11*, 3762.
(45) Salgueirino-Maceira, V.; Liz-Marzan, L. M.; Farle, M. *Langmuir* **2004**, *20*, 6946.
(46) Lin, L. W.; Kou, Y.; Zou, M.; Yan, Z. *Phys. Chem. Chem. Phys.* **2001**, *3*, 1789.
(47) Wong, S. T.; Lee, J. F.; Cheng, S.; Mou, C. Y. *Appl. Catal., A* **2000**, *198*, 115.
(48) Turek, W.; Spiechota, A.; Haber, J. *Catal. Lett.* **2009**, *127*, 7.
(49) Alyea, E. C.; Keane, M. A. *J. Catal.* **1996**, *164*, 28.
(50) Allard, L. F.; Flytzani-Stephanopoulos, M.; Overbury, S. H. *Microsc. Microanal.* **2010**, *16* (4), 375.
(51) Rim, K. T.; Eom, D.; Chan, S. W.; Flytzani-Stephanopoulos, M.; Flynn, G. W.; Wen, X. D.; Batista, E. R. *J. Am. Chem. Soc.* **2012**, *134*, 18979.
(52) Jin, M.; Cheng, Z. M. *Catal. Lett.* **2009**, *131*, 266.